JOM
https://doi.org/10.1007/s11837-022-05297-x

Composition and Structure Analysis of Hard Grey Scale (HGS) Formed on Cold Surfaces Exposed to Aluminium Production Off-gas

DANIEL PEREZ CLOS ,[1,4] HANNES ZEDEL,[1] SVERRE GULLIKSTAD JOHNSEN,[1,2] PETTER NEKSÅ,[3] and RAGNHILD ELIZABETH AUNE[1]

1.—Department of Materials Science and Engineering, Norwegian University of Science and Technology (NTNU), 7034 Trondheim, Norway. 2.—SINTEF Industry, 7031 Trondheim, Norway. 3.—SINTEF Energy Research, 7034 Trondheim, Norway. 4.—e-mail: danipclos@gmail.com

Hard grey scale (HGS) is a strongly adhering fouling material forming on solid surfaces impinged by off-gas generated in the pot cells of primary aluminium production plants. Even though associated maintenance costs have a significant economic impact, the mechanisms behind HGS formation are not well understood. In the present work, a cooled fouling probe or "cold finger" placed in the off-gas duct, upstream of the gas treatment centre (GTC), at a Norwegian aluminium production site was used to study the formation mechanisms of HGS. Fouling experiments were performed with durations ranging from a few hours to several months. HGS formed on the windward side of the probe, whereas dusty and loosely attached deposits accumulated on the leeward side. The chemical composition and crystal phase evolution of the different deposits and off-gas particle samples were analysed by electron probe micro-analyser equipped with an energy-dispersive spectrometer (EPMA-EDS), quantitative x-ray diffraction (Q-XRD), LECO-C and transmission electron microscopy (TEM). Moreover, image analysis (IA) was used to investigate the particle size distribution and deposition properties of particles with different compositions. Inertial deposition of atmolite ($NaAlF_4$) nanoparticles, produced by pot cell electrolyte vapour condensation, has been identified as the key mechanism in the formation of HGS.

INTRODUCTION

In the present work hard grey scale (HGS) specifies a type of particulate fouling that occurs in systems transporting the off-gas generated from the aluminium production electrolysis cells. The term scale probably derives from the hard and compact layers that HGS forms, which are similar to scaling processes, also known as precipitation fouling, where a supersaturated component in a fluid crystallizes on a cold surface.[1]

HGS is reported to form in areas where particles impinge on a solid surface because of the large curvature of fluid streamlines and can grow in large aspect ratios. This is especially problematic in dry scrubber components and pipe bends. Dry scrubbers use "primary" or smelter grade alumina (SGA) to absorb hydrogen fluoride (HF) from the off-gas by means of fluidized beds or injection systems.[2] The reacted "secondary" alumina, which is mixed with the off-gas particles captured in the filter bags, is partly recycled to the dry scrubber and partly transported to the pot cells by pneumatic conveyors.

A different type of HGS forms in the secondary alumina transport pipes, which has a brighter grey colour than HGS collected in off-gas systems.[3,4] The fact that primary alumina transport pipes do not

(Received January 21, 2022; accepted March 28, 2022)

Published online: 27 April 2022

suffer from HGS formation clearly indicates that a key component from the off-gas must trigger HGS growth in secondary alumina streams.

The nature of HGS has been studied by several researchers leading to various suggested formation mechanisms based on particle re-crystallization[3,5] and inertial deposition of highly adhesive submicron particles[6,7] and formation of a binder phase.[4] The latter was suggested by Haugland et al.[4] who monitored the growth of HGS in a secondary alumina pipe for 4 months. In their study, correlations between HGS growth rates and different operational parameters were reported. Parameters increasing pot cell emissions (i.e., anode effects) or temperature were found to enhance HGS growth rates. Transmission electron microscope (TEM) observations indicated that HGS consisted of submicron alumina particles with an accumulation of C and Na at the intergranular region. Furthermore, atomic force microscope (AFM) measurements revealed that the intergranular region was softer and had stronger adhesion than the grains they surrounded. From these results it was suggested that a binder phase produced by either NaF-AlF_3 reactions or sodium hydroxide ($NaOH$) formation from Na_2O impurities reacting with moisture could act as adhesive between the particles.

To further elucidate the HGS formation mechanism, an extensive study on the composition and crystal phase characteristics of HGS collected in the surface of a fouling probe or "cold finger" has been performed by means of electron probe micro-analyser equipped with an energy-dispersive spectrometer (EPMA-EDS), LECO-C, quantitative x-ray diffraction (Q-XRD) and transmission electron microscopy (TEM) measurements. In addition, a deterministic image analysis (IA) method was applied for quantifying the particle size distribution and deposition characteristics of a heavy metal rich particle phase, and we compared the bulk particle behaviour.

Finally, an HGS sample from a secondary alumina transport pipe from the same aluminium plant produced in a previous project[4] was also analysed together with corresponding primary and secondary alumina samples and compared with the cold-finger HGS.

The fouling experiments were performed in a 2.4-m-diameter off-gas duct before the gas treatment centre (GTC), with an average off-gas velocity of 17.5 m/s[8] and an average dust load of 2.7 g/m[3][7]

METHODOLOGY

Sampling Methodology

A half-meter-long cylindrical cold finger was used in the present fouling experiments. The probe has a three tube-in-tube configuration with an outer diameter (tube 3) of 35 mm and a coolant flowing in the inner sections. Thermocouples (TC) and heat flux sensors (HF) placed on the surface of the centre tube (tube 2) allow for surface temperature and heat flux monitoring (see Fig. 1a). The outermost sleeve (tube 3), which was replaced after each experiment, covers and protects the sensors and is the substrate on which particle deposition occurs. More details on the cold-finger design can be found elsewhere.[9] Temperatures in the off-gas duct oscillated between 90 and 120°C from winter to summer depending on weather conditions.

Before starting the experiments, the coolant flow (pressurized air) was started, and the temperature and heat-flux logging system was initialized. The cold finger was then introduced to the off-gas duct through a flange opening upstream of the GTC. The probe was oriented in cross-flow with the off-gas. The nature and appearance of the deposits varied significantly around the cold-finger circumference as depicted in Fig. 1b. HGS formed on the front side of the cold finger (windward side) while loosely attached, dusty particles accumulated on the rear side (leeward side), which from here onwards will be referred to as "rear deposits". The term "cold-finger deposits" will be used when referring to both HGS and rear deposits.

To investigate the deposition rate as a function of time, a series of experiments with different durations was conducted. The exposure times ranged from 3 h to 8 months. At the end of each experiment, the cold finger was extracted from the flange and allowed to cool down by maintaining the coolant flow for about 2 min before removing the outer tube with the deposits.

The outer tube (tube 3 in Fig. 1a) was segmented transversally (black lines) into three pieces before the experiments, with fringes that allowed easy coupling and decoupling of the pieces.

The centre piece was then carefully separated to avoid loss of the loosely attached rear deposits. Thereafter, the piece was introduced in a specially

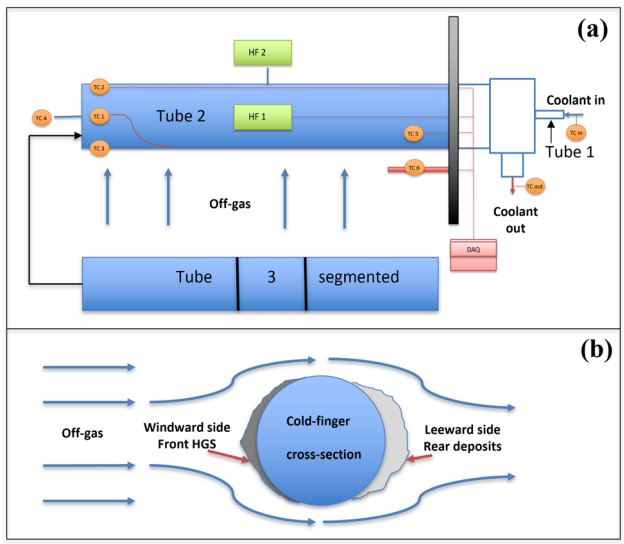

Fig. 1. Diagram showing the cold finger's sensor placement (a) and the deposit's location (b).

designed metal box, cast in epoxy, sliced and polished to analyse the pipe/deposit cross section by electron microscopy and IA. Samples from the front (front HGS) and rear (rear deposits) sides were scratched off from the two remaining pieces and collected in separate glass containers for analysis by XRD and LECO-C analysis. No indication that the morphology of the deposits varied along the length of the cold finger was observed.

Data from experiments of different durations ranging from a few hours to 8 months are presented in this study. Iso-kinetic sampling of the off-gas particles with particle collection on filters was performed on several occasions in a flange opening adjacent to the cold finger. The collected particles were suspended in epoxy and polished for electron microscopy analysis.

Scanning Electron Microscopy

A JEOL JXA-8500F EPMA was used for elemental quantification by EDS and to obtain secondary electron (SE) and back-scattered electron (BSE) micrographs analysed by IA. An acceleration voltage of 15 kV was used with 20-nA beam. EDS scans were performed at a scan magnification of 1000 ×, which allowed for a representative area to be analysed. Five off-gas samples, 14 front HGS samples, 9 rear deposit samples and one HGS sample from a secondary alumina transport pipe were analysed with this method. Samples from all different time scales (i.e. from 3 h to 8 months) were analysed by this technique.

LECO Analysis

A CS744 LECO-C instrument was used to quantify the levels of C in the different samples. The samples were ground with a mortar before being introduced into the instrument where the sample was combusted to release the carbon (C) as CO_2, which was detected with a non-dispersive infrared (NDIR) cell. Two off-gas samples, six front HGS samples and five rear deposit samples were analysed with this method. Samples from time ranges between 15 days and 3 months were analysed by this technique.

XRD Measurements

A D8 da Vinci XRD diffractometer from Bruker with a Lynx Exe XE-T detector was used to characterize the crystal phases of the secured samples. Additional measurements with a D8 advanced diffractometer with Lynxeye-2 detector were also performed with the same preparation and measurement settings to ensure comparability of the results. The scans were performed from 6 to 70° (2θ), with a step size of 0.011°/step and a scanning time of 0.6 s/step. A divergence slit opening degree of 0.3° was used. All samples were ground in a mortar to particle sizes suitable for powder diffraction analysis before being pressed into glass disk sample holders. Quantification of the samples was performed using the Rietveld refinement method with the TOPAS software.[10] Seven off-gas samples, 11 front HGS samples, 10 rear deposit samples and 1 HGS sample from a secondary alumina transport pipe were analysed with this method. Samples from time ranges between 15 days and 6 months were analysed by this technique.

TEM Measurements

Cross-sectional TEM lamellas were prepared from selected regions of tube/HGS cross sections from two samples using a FEI Helios G4 UX focused ion beam (FIB). Carbon or platinum protection layers (the first part of the layer made by e-beam assisted deposition to avoid ion-beam induced surface damage) were deposited on the selected regions prior to milling out the TEM lamella. Coarse thinning was performed at 30 kV acceleration voltage. The last part of the thinning was performed at 5 kV and finally 2 kV to minimize ion beam-induced surface damage on either side of the TEM lamellas.

TEM analysis was then performed using a double Cs aberration corrected cold FEG JEOL ARM 200F, operated at 200 kV and equipped with a large solid angle Centurio SDD (0.98 sr) EDS analysis and a Quantum ER GIF for dual electron energy loss spectroscopy (EELS). Two samples from a 15-day and 6-month experiment, respectively, were analysed by this technique.

Image Analysis (IA)

A deterministic IA method (described in detail elsewhere[11]) was used to analyse SE and BSE microscope images of deposits and off-gas particle samples to quantify particle size distributions. These results were used to calculate particle capture efficiencies for front HGS and rear deposits using $\overline{\eta} = \frac{\pi}{2}\frac{\overline{J}}{u_{bulk}C_p}$, where $\overline{\eta}$ is the averaged capture efficiency, $\overline{J}$ is the time and area averaged deposition flux (both for front HGS and rear deposits), u_{bulk} is the off-gas bulk velocity, and C_p is the particles concentration in the off-gas. The particle size-dependent capture efficiency $\overline{\eta}_i$ was then calculated using $\overline{\eta}_i = \frac{m_{i,d}}{m_{i,off}}\overline{\eta}$, where $m_{i,d}$ and $m_{i,off}$ are the deposits and off-gas particle size distributions, respectively. More details on this method are described in a previous work by the authors.[7] In addition, a heavy metal rich particle phase was analysed analogously, using the different contrast of this phase in BSE electron images. Samples from all different time scales (i.e. from 3 h to 8 months) were analysed by this technique.

RESULTS AND DISCUSSION

Chemical Composition Analysis

The off-gas has a large polydispersity, as can be seen in Fig. 2a where SE micrographs of off-gas particles are displayed. As was discussed in a previous study,[6] most of the larger particles that can be seen in the low magnification image (A) have irregular shapes with compositions corresponding to alumina particles (point EDS). In addition, a lower number of spherical particles is also present with compositions similar to that of the cryolite (Na_3AlF_6) bath.

Moreover, it is possible to observe grey diffuse structures like the one highlighted by the yellow square. The high magnification image (Fig. 2b) of such an area reveals a finely dispersed cluster of sub-micron particles. As was shown by Gaertner et al.,[12] the sub-micron phase in the off-gas consists mainly of atmolite ($NaAlF_4$) condensed vapours formed during the electrolyte vapour quenching.

In Fig. 3, EPMA images of a typical HGS (images D-F) and rear deposit (images A-C) samples are shown. The high contrast of a heavy metal rich particle phase in the BSE images allowed for a differentiation between this phase (green) and the other particles (red). We previously demonstrated[6] that those particles were rich in Fe, Ni and S. In addition, three examples of C particles are highlighted by yellow squares in Fig. 3c. Due to the similar atomic density between C particles and C-based epoxy resin, the contrast between them is not strong enough for the C particles to be segmented using IA.

Table I shows the chemical composition of off-gas samples and cold-finger deposits (front HGS and rear deposits) as well as primary and secondary alumina and HGS from a secondary alumina transport pipe, obtained from Haugland et al.[4] The last column displays the estimated Ni plus Fe wt.% from the heavy metal rich particles (green particles in image Fig. 3c, f) measured by IA. Correction factors were applied to consider Ni-Fe content in these particles (60% measured by point EDS[6]) and density ratio between heavy-metal particles (NiS: 5800 kg/m^3) and the weighted average density of the main crystal phases measured by XRD in this work (3596 kg/m^3). This was done to transform volume % values obtained from IA measurements to wt.% values measured by EPMA. No time dependence was observed in HGS and rear deposit average compositions, with standard deviation for the main elements (Al, Na, F and O) across different samples between 4% and 15%.

As can be seen from Table I:

- Both front HGS and rear deposits have a similar chemical composition regarding the main elements. However, HGS has higher levels of Fe and Ni (64% and 31%, respectively) and lower amounts of C (61%) than the rear deposits. The lower amount of C in HGS is believed to be due to the C particle sizes (like the ones highlighted in Fig. 3c), not being abundant in HGS samples.
- The summed concentrations of Ni and Fe in the off-gas are 80% lower than in front HGS and 70% lower than in the rear deposits. These values compare well with the results from IA of the heavy metal rich particles. Results for front HGS and rear deposits deviate only by 20% and 15%, respectively. Deviation for the off-gas case is a bit higher (50%) but still acceptable considering the large standard deviations in heavy metal particle content between different off-gas samples (104.2%). These results indicate that the Fe and Ni are mainly present in the form of these heavy metal and S-rich particles. These particles are believed to be formed from impurities in the carbon anodes, which are also the main source of S as was discussed by Jahrsengene et al.[13]
- The off-gas particles also have larger aluminium

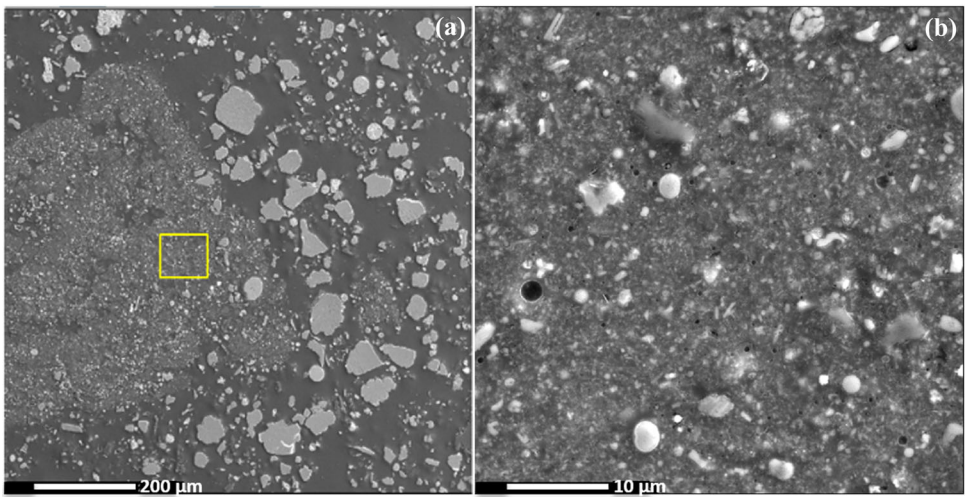

Fig. 2. SE images of an off-gas powder suspension in epoxy for 40 × magnification (a) and a 2000 × magnification area from the submicron particle clusters area (b) like the one highlighted by the yellow square in image A (Color figure online).

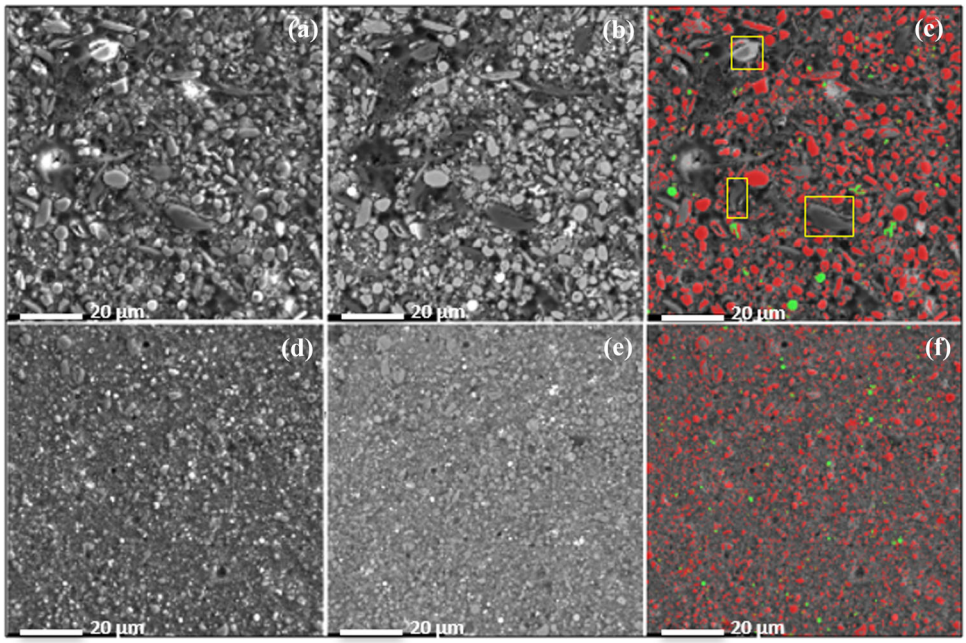

Fig. 3. SE images (a, E and BSE images (c, f) of a typical rear deposit sample (a-c) and an HGS sample (d-f). The particle segmentation is divided in sodium fluoroaluminates and alumina particles (red) and heavy metal rich particles (green). Examples of carbon particles are highlighted by yellow squares in image C (Color figure online).

Table I. Average composition in wt.% for different types of samples by EPMA-EDS and C content by LECO-C (the EDS values have not been normalized with LECO-C results)

Sample	N° samples	Al	Na	F	O	S	Ni	Fe	Ca	C	IA (Ni+Fe)
Off-gas all	5 (2)	37.3	7.5	19.7	28.9	3.2	0.5	0.4	0.4	(6.2)	1.5
Off-gas clusters	5	26.6	13.6	28.5	23.8	5.8	0.4	0.4	0.5	–	–
Front HGS	14 (6)	32.6	10.3	27.9	19.3	4.1	2.1	2.3	0.7	(3.3)	3.4
Rear deposits	9 (5)	27.8	11.9	30.8	19.8	5.0	1.6	1.4	0.9	(8.4)	3.5
[a]Primary alumina	–	52.7	0.0	0.0	46.8	0.0	0.0	0.0	0.0	–	–
[a]Secondary alumina	–	50.6	0.6	1.7	45.7	1.1	0.0	0.0	0.0	–	–
2nd alumina HGS	1	43.9	5.7	14.5	30.4	3.7	0.6	0.4	0.3	–	–

The last column displays the Ni+Fe elemental composition obtained from IA results. [a](Private communication, Morten Isaksen, M., Hydro Aluminium, Norway, Nov. 2020).

and oxygen concentrations compared with the deposits, which can be explained by the larger non-depositing alumina particles entrained during alumina feeding.

- The composition of the off-gas sub-micron particle cluster areas (see Fig. 2b) is similar to the deposits for the main elements and also for S, which has also been shown to accumulate in the finer off-gas particle fractions.[14] Such small particles have a large surface-to-volume ratio where gaseous S species can be adsorbed in higher volumetric concentrations. Therefore, the increase in S content in HGS and rear deposits can be explained by the larger amounts of small particles. The high levels of oxygen in these small-particle cluster areas point to a partial hydrolyzation of atmolite gas, which will be further discussed in "High-Annular Dark Field (HADF-TEM) Element Mapping" section.
- The composition of HGS from secondary alumina transport pipes is enriched in Na, F and S compared with the secondary alumina it is produced from. This result will be further discussed in "Crystal Phases From Quantitative X-ray Diffraction (Q-XRD)" section.

Particle Deposition Mechanisms

The heavy metal rich particles (green phase in Fig. 3) offer an alternative way of studying the particle deposition characteristics in the cold-finger deposits that can be compared with the "all

particles" case (red + green phases in Fig. 3c, f) previously reported.[7]

Figure 4 shows the particle size distribution of the heavy metal rich particles in the cold-finger deposits and in the off-gas with a maximum particle size of 10 μm. The fact that $>$ 80 wt.% of the off-gas particles have sizes $>$ 10 μm[7] strongly suggests that the enrichment of Fe and Ni in the deposits is due to similar particle sizes of this phase in the off-gas and in the deposits.

The figure also shows the large number of metallic particles in HGS with sub-micron sizes ($>$ 50 % in volume), which, as has been mentioned, allows for a closely packed structure with the corresponding bulk properties in terms of hardness and adhesion.

The capture efficiencies for the heavy metal rich particles are shown in Fig. 5 for the front (A) and rear (B) sides. In addition, results considering all particles and particle impaction efficiency results by Haugen and Kragset[15] using direct numerical simulation (DNS) are also displayed. The simulated impaction efficiency results account for the fraction of particles approaching the cold finger's projected area that would impact the cold-finger surface, whereas capture efficiency results account for the fraction of particles that actually sticks to the surface of the cold finger.

Figure 5 shows that the capture efficiencies for small particles (*i.e.* Stokes numbers $<$ 0.1) are in good agreement with the numerical impaction efficiencies suggesting high adhesion probabilities at these particle sizes. For larger particles (*i.e.* Stokes number $>$ 0.1), re-bounding and re-entrainment effects[16,17] result in lower capture efficiencies than the impactions predicted by the simulations.

The heavy metal rich particles follow the same trends in capture efficiencies as the "all particles" case, on both the front and rear sides. However, the values are lower for the heavy metal rich particles.

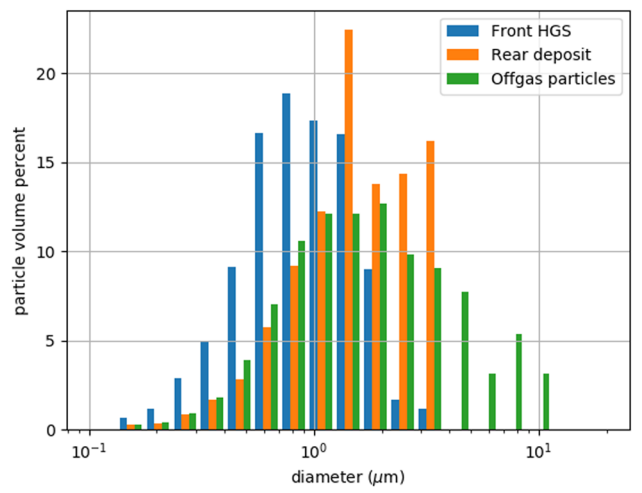

Fig. 4. Particle size distribution from IA particle segmentation of the heavy metal rich particles in the off-gas and cold-finger deposits.

The following considerations are made to explain this difference.

Given the small particle sizes in the deposits, we assume zero particle-fluid relative velocities for all particle sizes. From this, it can be calculated that the ratio of both particle inertia I and diameter d for particles with the same Stokes numbers and different densities ρ is $\frac{I_1}{I_2} = \frac{d_1}{d_2} = \sqrt{\frac{\rho_2}{\rho_1}}$. This means that the heavy metal rich particles approach the wall with approximately 20% less inertia and smaller diameters than the other particles with the same Stokes numbers. These observations are in agreement with the *interception mechanism* described in the study by Haugen and Kragset,[15] where they showed that in the low Stokes numbers regime, the particles follow the streamlines and therefore are *intercepted* by the wall due to their finite size. They also showed that larger Reynolds numbers (i.e. particle inertia) at this regime resulted in increased impaction efficiencies because of viscous effects becoming important for small particles in the wall boundary layer. Thus, both the lower inertia and diameter of the heavy metal rich particles contribute to their lower impaction and ultimately capture efficiencies.

These results strongly support the hypothesis of inertial deposition of small particles as the main mechanism in the formation of HGS.

TEM Analysis of HGS Structure

TEM results are presented in this section to investigate HGS structure and composition details.

Bright Field (BF-TEM)

BF-TEM images from two samples are displayed in Fig. 6. In BF-TEM mode the electrons go through the sample and into the detector. Therefore, the contrast is the opposite from the BS-EPMA images displayed in "Chemical Composition Analysis" section. This means that the white areas are holes, whereas the black spots correspond to the heavy metal rich particles.

Figure 6a depicts an HGS sample extracted from a tube-HGS interface. Figure 6b And c are low and high magnification images from an HGS sample taken close to the HGS/off-gas interface (recently deposited). From the image it is possible to see that the HGS from the outer layer has a high granular morphology with clear separated boundaries between the highly heterogeneous types of particles. In Fig. 6c particles with different morphologies and compositions similar to cryolite (1, 2), alumina (3, 4) and heavy metal rich particles (5) are highlighted. In contrast, the inner layer close to the metal surface (Fig. 6a) has a more compact morphology suggesting that the different particles from the left image were compressed together. This could be an aging effect caused by the aerodynamic pressure of the off-gas in the front side of the cold finger

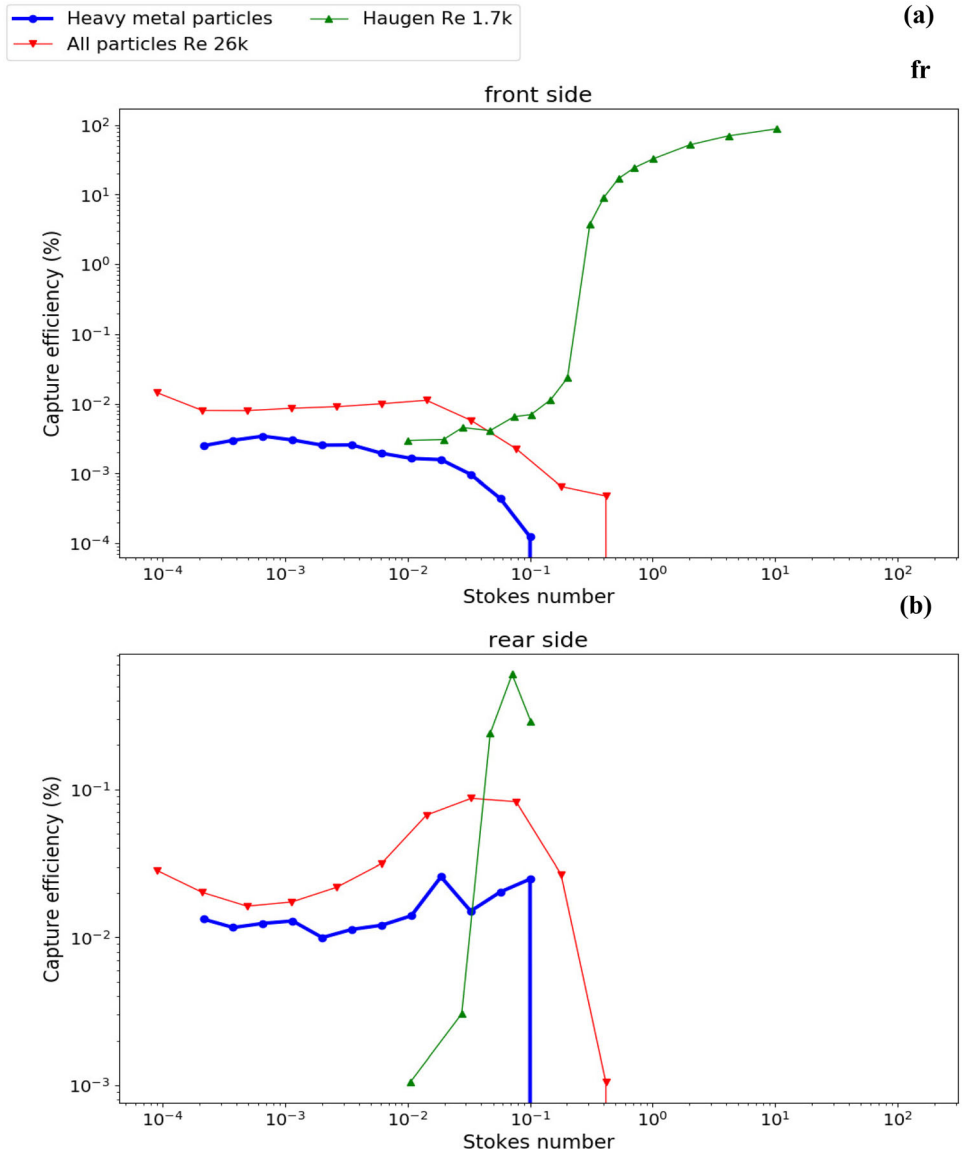

Fig. 5. Capture efficiencies for front HGS (above) and rear deposits (below) for the heavy metal rich particles (green phase as in Fig. 3), the case with all particles (green + red phases as in Fig. 3) and impaction efficiency simulation results from Haugen and Kragset.[15] Average particle Reynolds number in experiments and simulations displayed in the legend (Re) (Color figure online).

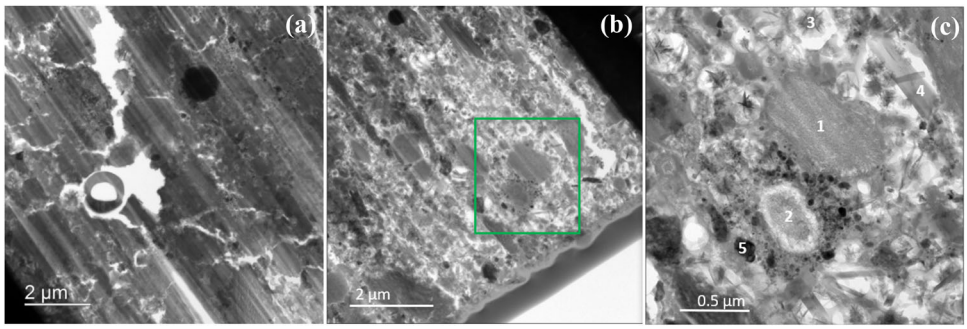

Fig. 6. BF TEM images of an HGS inner layer close to the metal interface (a), an outer layer close to the off-gas side (b) and the zoomed-in area in image (b), highlighted with the green square (c) (Color figure online).

combined with the particle impaction from the non-depositing larger particles.

High-Annular Dark Field (HADF-TEM) Element Mapping

In Fig. 7, HADF-TEM images from three areas of two HGS samples are depicted, with different spots indicated by numbers. The elemental composition in these spots is shown in Table II. In this technique, as opposed to BF-TEM, black areas correspond to holes in the sample.

Figure 7a depicts an HGS sample close to the metal tube-HGS interface (same sample as in Fig. 6a). The metal tube (purple) can be seen on the top left corner. A gap was always present along the HGS-metal interfaces of the different experiments. Thermal stresses in the tube/HGS interface upon probe cooling and/or humidity absorption-induced swelling of HGS are likely responsible for this detachment. As Fig. 7a also shows, the green layer where the HGS particles grow (point 1) is mainly an iron oxide layer. Such an oxide layer between the HGS and tube interface was also reported in the work by Haugland et al.[4] From electron diffraction analysis, it was established that it corresponds to an amorphous iron oxide layer. It is not quite clear whether such an oxide layer is formed prior to particle deposition or at a later stage but HGS particles appear to be entwined in it. Points 2 and 3 have compositions of alumina and cryolite bath particles, respectively. Na (yellow) appears to have diffused away from the cryolite-like particle and into the iron oxide phase.

Figure 7b is also from the same metal tube-interface sample as in Fig. 7a. Electron diffraction analysis of points 3 and 4 reveals that they consist of cryolite crystals, which showed certain instability under the electron beam, resulting in the Na-enriched granularity of the surface of those particles. Point 5 corresponds to an alpha-alumina (corundum) particle.

Another type of particle that is quite abundant in HGS is the fibrous flower-like alumina particles, sometimes enriched in Fe like the one in point 6 (or point 3 in Fig. 6c). Electron diffraction of this and other similar particles revealed a face-centred cubic structure corresponding with the meta-stable *eta* phase of alumina. This type of structure was argued by L'vov et al.[18] to be formed by hydrolysis of the outer regions of the bath vapour flow in contact with the dilution air humidity. This can also explain the large levels of oxygen in the submicron particle clusters displayed in Table I. Such fibrous alumina nano-particles were identified in the pot room and in the respiratory tracts/lungs of potroom workers; whilst there may be potential health impacts and linkages to respiratory disease, these links are still the topic of much investigation.[19–21]

Point 7 in Fig. 7b corresponds to a region with accumulation of metallic particles rich in Fe, Ni, V (not shown in Table I) S, C and P. The white particles are rich in Ni and S whereas the purple ones have Fe and S as the main elements. As was discussed in "Chemical Composition Analysis" section, these particles likely originate from carbon anode impurities.

Figure 7c is taken from a region close to the HGS-air interface. As discussed above, this sample has a more granular and porous structure. Most particles have a composition close to either cryolite-like (point 8) or alumina (point 9) particles. Electron diffraction analysis of particles similar to point 8 revealed the presence of atmolite phase although it was extremely unstable under the electron beam, decomposing into AlF_3 and some Na-rich species that could not be identified. The Na rich aggregates can be seen all over the image as yellow dots.

These results support the initial hypothesis that HGS is formed by inertial deposition and compaction of small particles of highly heterogeneous morphology and composition. No indication of binder phases was found in the intergranular region of the larger particles, and no sintering was observed that could suggest individual particles re-crystalizing into larger crystals.

Crystal Phases From Quantitative X-ray Diffraction (Q-XRD)

Table III shows the Rietveld-based Q-XRD average results in wt.% for the main crystal phases of

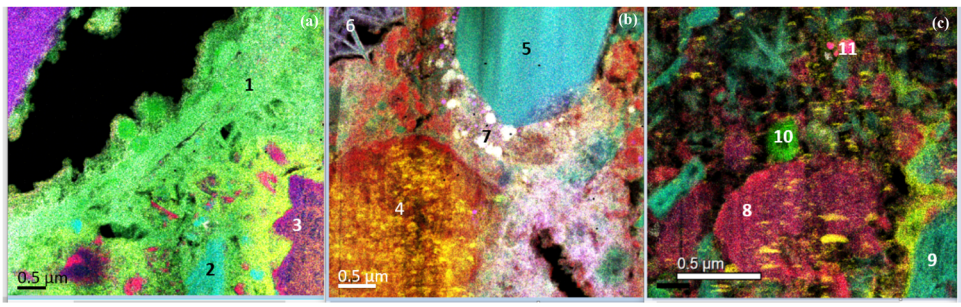

Fig. 7. EDS element colour map from HADF-TEM analysis: a HGS/metal tube interface, b near HGS/metal tube interface, c near HGS/air interface. Al: blue, Na: yellow, O: light green, F: red, S: white, Fe: purple, C: dark green. The numbers indicate local composition areas displayed in Table II (Color figure online).

Table II. Elemental composition of different areas marked in Fig. 7 in wt.%

Point in map	Al	Na	F	O	S	Fe	Ni	C	P
Point 1	11.5	1.1	0	44.5	6.4	29.0	0.9	6.4	0.2
Point 2	44.6	0	0	46.9	1.4	5.3	0	1.8	0
Point 3	52.5	13.1	32	0	0	0.6	0	1.8	0
Point 4	29.3	25.4	35.6	6.8	0.5	0.9	0.1	1.5	0
Point 5	62.5	0	0	36.9	0	0.4	0	0.8	0.2
Point 6	29.7	1.1	0	38.9	2.3	24.3	1.1	2.5	0.1
Point 7	18.0	6.3	11.2	14.5	5.3	15.2	17	7.5	4.9
Point 8	39.5	3.8	45.3	9.5	1.3	0.1	0	0.3	0
Point 9	52.1	0.7	4.7	41.4	0.2	0.1	0.1	0.4	0.1
Point 10	10.9	5.1	13.8	5.8	0.7	0.2	0	62.6	0
Point 11	10	4.9	8.5	6.9	0	44.1	9.2	5.2	11.2

Table III. Q-XRD results for the average of the main crystal phases in wt.%

Crystal phase	Off-gas	Front HGS	Rear deposits	HGS 2nd alumina	Primary alumina	Secondary alumina
No. samples	7	11	10	1	1	1
Total alumina	63.6	39.5	33.8	75.9	100	100
Na_3AlF_6 (cryolite)	4.9	1.0	8.7	–	–	–
$NaAlF_4$ (atmolite)	4.1	32.9	11.1	18.0	–	–
$Na_5Al_3F1_4$ (chiolite)	4.5	9.8	10.0	1.4	–	–
C (graphite)	18.3	0.8	31.5	–	–	–
Other minor phases	4.7	11.6	4.7	4.6	–	–
Al_2O_3 (alpha)	8.1	18.9	9.6	43.3	1	1
Al_2O_3 (theta 5-10 nm)[a]	25.7	15.7	14.5	21.9	75	70
Al_2O_3 (theta 30 nm)[a]	14.4	2.0	1.3	2.1	5	6
Al_2O_3 (eta)[a]	15.4	2.9	8.4	8.6	19	23

[a] Crystal phases from the study by Zhoug and Snyder.26 Average size of some crystallite phases displayed in nm

the cold-finger deposits, off-gas particles as well as the HGS sample from a secondary alumina transport pipe obtained from the study by Haugland et al.[4] together with primary and secondary alumina samples. All samples were analysed under the same conditions in the present study. No time-dependent trends were observed for any of the phases as a function of time. Standard deviation average values for the main crystal phases across different samples of the same type (i.e. HGS, rear deposits and off-gas particles) vary between 4 and 17%.

The most relevant result reported in Table III is the large level of atmolite in both types of HGS. This indicates that atmolite is the Na-rich binding material that was found in the intergranular region between the alumina particles that was reported by Haugland et al.[4] to form the HGS. The fact that fluorine (F) did not accumulate in the intergranular interface can be explained by HF gas absorption, which can penetrate the alumina particles' porous structure. A zoomed-in look at the Na mapping presented in the work by Haugland et al.[4] reveals a small granular texture with particle sizes in the range of tens of nm.

These atmolite nanoparticles have been shown to originate from the pot cell's electrolyte vapour condensation in the off-gas.[22] They are captured in the dry-scrubber filters and periodically re-entrained in the secondary alumina stream. The deposition of these nanoparticles is believed to be the key component in HGS formation by filling up the void between the larger depositing particles and thus generating a closely packed structure that explains the HGS bulk hardness and surface adhesion properties.

The differences in chemical composition between the two types of HGS can be explained by the types of particles with relevant sizes for deposition ($\approx$0.05-5 μm), which are different in the two streams. Alumina is the main phase in secondary alumina, whereas a mixture of alumina fines and

electrolytic bath particles [i.e. cryolite, chiolite ($Na_5Al_3F_{14}$) and atmolite] dominates the off-gas composition.

No atmolite was detected in the secondary alumina sample, which is partly due to the low concentration of this phase (< 3 wt.% considering Na absorption in secondary alumina measured by EDS, see Table I) and partly due to the large background introduced by the theta alumina phase with low crystallite sizes, which makes detection of minor phases difficult.

The total amount of alumina in the off-gas is 27% larger than both front and rear deposits because of the larger fraction of alumina particles that do not deposit, as previously discussed.

It can also be seen that the stable alpha-alumina phase (corundum) is enriched in HGS as was also previously reported.[4] The levels of corundum in the raw alumina supplied to the pot cells are kept as low as possible (3 wt.% on average*) given the low dissolution rates of this phase in the bath. The final step in alumina production by the Bayer process involves calcination of the gibbsite ($Al(OH)_3$) precipitated crystals at 1000°C to produce the amorphous transition alumina phases used in aluminium production.[23] It is to be expected that only the smallest gibbsite particles can reach the final stable corundum crystal phase during that process. This explains the increased concentration of alpha alumina in the off-gas compared to secondary alumina as the smaller particles are more entrained by the off-gas during the feedings of alumina to the pot cells. This is also in agreement with the enrichment of alpha alumina in both types of HGS as the particle sizes of these materials correspond to the smallest size fraction of alumina particles in either the off-gas or secondary alumina streams.

The relative amounts of graphite between the off-gas and the cold-finger deposits agree with those measured by LECO-C as shown in "Chemical Composition Analysis" section. However, the absolute amounts are much higher in the Q-XRD measurements.

Cryolite levels in HGS are much lower than in the rear deposits and off-gas particles as was also reported in previous studies.[5,6] Cryolite liquid droplets from the electrolytic bath are entrained by the off-gas because of anode-produced CO_2 bubbling.[24] The size of these droplets is in the range of a few micrometres, which is abundant in rear deposits but scarce in the smaller-sized particles in front HGS.

Chiolite is enriched in both front HGS and rear deposits in similar amounts compared to the off-gas. This suggests that chiolite particle sizes are between the average particle sizes from HGS and rear deposits. Such small particle sizes can be explained as part of atmolite vapour condensation in the hot areas (> 800°C) of the off-gas as was observed in the laboratory experiments by Hung and Metson.[25] Aluminium fluoride (AlF_3), which is a by-product in the formation of chiolite from atmolite, is not shown in the table given the low amounts detected in most samples (< 1 wt.% except for HGS samples with an average of 1.9 wt.%).

Several minor phases (around 20) with concentrations < 1 wt.% are also present in the different samples (among others NiS, $AlNaO_2$, $Al(OH)_3$, AlF_3, $NaCaAlF_6$, metallic Fe-Ni and S_{12}). No signs of accumulation in HGS samples have been established that could suggest the presence of a specific binder phase. Moreover, the concentration of the main crystal species is relatively constant over time. This means that similar levels have been found for samples grown over the course of a few days, several weeks or months, which supports the hypothesis that no re-crystallization phenomena occur in HGS formation.

It should also be mentioned that the low size of the crystallites gives an appearance of large background commonly present in samples with high amorphous content. However, the use of an internal standard in Q-XRD analyses revealed that the levels of amorphous content in the different samples were similar and < 5 wt.%, which also rules out the possibility of an amorphous-based binder phase.

The absence of a binder phase and particle recrystallization leads to the conclusion that the close packing of small particles results in the hard and highly adhesive properties of HGS.

HGS Layers and Process Operation

EPMA images of an HGS sample from a 6-month experiment are displayed in Fig. 8. As can be seen from the figure, the HGS structure is clearly stratified. Compositional analysis (EDS) of the different layers shows no significant differences between them except for the outer layer, which has larger amounts of C (5 wt.%) than the others (2 wt.%). Discussions with the industry revealed that in the period in which the last layer grew, an alumina batch with an excess of fines had been used. This observation indicates that changes in raw materials might be a relevant factor in the formation of such distinctive layers. It must be stated that the large differences between the layers that can be seen in the SE image (image B) are mainly topographic, which means that the brighter layers are clumps of particles that are protruding more in the cross section resulting in hills that darken the surrounding valleys.

SUMMARY AND CONCLUSIONS

The formation of HGS in aluminium production off-gas systems has been studied by running HGS-gathering experiments in a cold finger with durations ranging from a few hours to 8 months. HGS formed in the windward side of the probe whereas dusty and loosely attached deposits accumulated on the

*Industrial data provided by project partners.

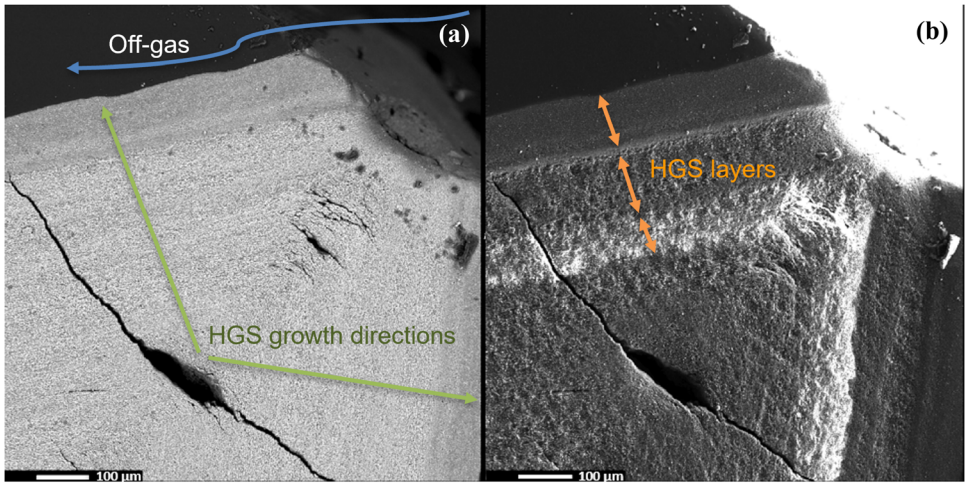

Fig. 8. BSE (**a**) and SE **b** images of an HGS sample gathered over the course of 6 months.

leeward side (rear deposits). Details on cold-finger HGS chemical composition and crystal structure are presented and compared with off-gas particles, rear deposits as well as an HGS sample from a secondary alumina transport pipe. IA of electron micrographs was used to characterize the particle size distribution and deposition characteristics of a heavy metal rich particle phase. The results were compared with the bulk behaviour of the particles and a modelling study from the literature.

The chemical composition and particle sizes of HGS samples were found to be similar to the submicron particle clusters observed in off-gas particles, which originate from the condensation and hydrolysis of electrolytic bath vapours (atmolite) from the aluminium production pot cells. Moreover, the enrichment of Ni, Fe and S in the cold-finger deposits has been tailored to the heavy metal rich particulates because of the similar size range of this phase and the depositing particles. Those particles, which are reported from literature studies to originate from the carbon anodes consumption in the pot cells, are thus believed to be circumstantially enriched in both HGS and rear deposits without necessarily playing a key role.

TEM results revealed a more granular and porous structure at the layers closer to the off-gas/HGS interface than in the layers close to the HGS/tube interface. This suggests a mechanical compaction process of the already deposited particles caused by the off-gas dynamic pressure at the front side of the probe. No sintering between HGS particles was observed by TEM that could suggest particle recrystallization.

The softer Na-rich intergranular material with higher adhesive properties in the HGS from secondary alumina transport pipe previously reported has been identified as atmolite nanoparticles by Rietveld-based quantitative XRD analysis. Atmolite is also present in large amounts in the cold-finger HGS. The deposition of atmolite-enriched submicron particles in HGS is thus believed to be the key to a closely packed structure that results in the hard and highly adhesive nature of HGS.

Given the similar trends in capture efficiencies between a heavy metal rich particle phase and the rest of the particles, with good correlation with DNS-based simulations, it is concluded that inertial particle deposition of sub-micron rich particles is the main mechanism behind the formation of HGS.

From the present results it can be argued that the formation of HGS could be avoided if the particle size distribution of the condensed electrolyte vapours could be significantly increased. This could be partially achieved by using preheated dilution air to generate the off-gas, reducing the quenching effect. Reducing the volume of dilution air would also result in more concentrated vapours producing larger condensed particles. Such strategies would need to be followed by extra cooling of the pot cells as well as the off-gas before reaching the GTC. The increased off-gas temperatures would at the same time offer a more attractive heat recovery potential.

ACKNOWLEDGEMENT

The present work has been funded by the SFI Metal Production (Centre for Research-based Innovation, 237738), and the authors gratefully acknowledge the financial support from the Research Council of Norway and the partners of the SFI Metal Production. The authors also gratefully acknowledge the contributions of Morten Peder Raanes for the analysis of EPMA samples, Per Erik Vullum for the analysis of TEM samples as well as Daniel Jansen and Nicholas Fobbe for the analysis of XRD samples.

FUNDING

Open access funding provided by NTNU Norwegian University of Science and Technology (incl St. Olavs Hospital - Trondheim University Hospital).

CONFLICT OF INTEREST

On behalf of all authors, the corresponding author states that there is no conflict of interest.

OPEN ACCESS

REFERENCES

1. S.F.E. Boerlage, *Scaling and Particulate Fouling in Membrane Filtration Systems*, Taylor & Francis (2001).
2. S. Lindsay and N. Dando, *Light Met.*, 275 (2009).
3. N.R. Dando and S.J. Lindsay, *Light Met.*, 227 (2008).
4. I. Bock Haugland, O. Kjos, A. Røyset, P.E. Vullum, A. Aarhaug, and M. Halstensen, *Light Met.*, 697 (2019).
5. H. Gaertner, A.P. Ratvik, and T.A. Aarhaug, in *Light Met.* Wiley, 547 (2014).
6. D.P. Clos, P. Nekså, S.G. Johnsen, and R.E. Aune, in *Light Met.*, 707 (2019).
7. D. Clos, H. Zedel, S.G. Johnsen, P. Nekså, and R.E. Aune, *J. Aerosol Sci.*, 161, 105946 (2022).
8. D.P. Clos, S.G. Johnsen, P. Nekså, and R.E. Aune, *Light Met.*, 710 (2020).
9. D.P. Clos, H. Gaertner, P. Nekså, S.G. Johnsen, and R.E. Aune, *Heat Exch. Fouling Clean.*, 261 (2017).
10. R.E. Dinnebier, A. Leineweber, and J.S.O. Evans, *Rietveld Refinement* (De Gruyter, Berlin, Boston, 2018).
11. H. Zedel, R. Fritzsch, S. Akhtar, and R. Aune, *Light Met.*, 1113 (2019).
12. H. Gaertner, A. P. Ratvik, and T. A. Aarhaug, in *Light Met.*, 839 (2012).
13. G. Jahrsengene, H.C. Wells, C. Sommerseth, A.P. Ratvik, L.P. Lossius, K.H. Sizeland, P. Kappen, A.M. Svensson, and R.G. Haverkamp, *Metall. Mater. Trans. B* 50, 2969. (2019).
14. H. Gaertner, A. P. Ratvik, and T. A. Aarhaug, in *Light Met.* Wiley, pp. 769–774 (2013).
15. N.E.L. Haugen and S. Kragset, *J. Fluid Mech.* 661, 239. (2010).
16. S. G. Johnsen and S. T. Johansen, in *Seventh Int. Conf. CFD Miner. Process Ind.*, pp. 1–6 (Unpublished, 2009).
17. S. Wall, W. John, H.-C. Wang, and S.L. Goren, *Aerosol Sci. Technol.* 12, 926. (1990).
18. B. V. L'vov, L. K. Polzik, S. Weinbruch, D. G. Ellingsen, and Y. Thomassen, *J. Environ. Monit.* 7, 425 (2005).
19. C. Voisin, F. Fisekci, B. Buclez, A. Didier, B. Couste, F. Bastien, P. Brochard, and J.C. Pairon, *Eur. Respir. J.* 9, 1874. (1996).
20. L. Fritschi, M.R. Sim, A. Forbes, M.J. Abramson, G. Benke, W.A. Musk, and N.H. de Klerk, *Int. Arch. Occup. Environ. Health* 76, 103. (2003).
21. G. Benke, M. Abramson, and M. Sim, *Ann. Occup. Hyg.* 42, 173. (1998).
22. H. Gaertner, A. P. Ratvik, and T. A. Aarhaug, in *Light Met.*, pp. 345 (2011).
23. H. Kvande, in *Fundam. Alum. Metall.*, edited by R. Lumley (Woodhead Publishing, 2011), pp. 49–69.
24. W. Haupin and H. Kvande, in *Light Met.* (1993).
25. J. H. Hung and J. B. Metson, in *Light Met.*, edited by A. Tomsett Springer, pp. 751–757 (2020).
26. R.-S. Zhou and R.L. Snyder, *Acta Crystallogr. B* 47, 617. (1991).